

RESEARCH ARTICLE

Deletion of *taf1* and *taf5* in zebrafish capitulate cardiac and craniofacial abnormalities associated with TAFopathies through perturbations in metabolism

Jamison Leid¹, Ryan Gray², Peter Rakita¹, Andrew L. Koenig¹, Rohan Tripathy¹, James A. J. Fitzpatrick³, Charles Kaufman^{4,5}, Lilianna Solnica-Krezel⁴ and Kory J. Lavine^{1,4,6,*}

ABSTRACT

Intellectual disability is a neurodevelopmental disorder that affects 2-3% of the general population. Syndromic forms of intellectual disability frequently have a genetic basis and are often accompanied by additional developmental anomalies. Pathogenic variants in components of TATA-binding protein associated factors (TAFs) have recently been identified in a subset of patients with intellectual disability, craniofacial hypoplasia, and congenital heart disease. This syndrome has been termed as a TAFopathy and includes mutations in TATA binding protein (TBP), *TAF1*, *TAF2*, and *TAF6*. The underlying mechanism by which TAFopathies give rise to neurodevelopmental, craniofacial, and cardiac abnormalities remains to be defined. Through a forward genetic screen in zebrafish, we have recovered a recessive mutant phenotype characterized by craniofacial hypoplasia, ventricular hypoplasia, heart failure at 96 h post-fertilization and lethality, and show it is caused by a nonsense mutation in *taf5*. CRISPR/CAS9 mediated gene editing revealed that these defects were phenocopied by mutations in *taf1* and *taf5*. Mechanistically, *taf5*^{-/-} zebrafish displayed misregulation in metabolic gene expression and metabolism as evidenced by RNA sequencing, respiration assays, and metabolite studies. Collectively, these findings suggest that the TAF complex may contribute to neurologic, craniofacial, and cardiac development through regulation of metabolism.

KEY WORDS: TAFopathy, TAF1, TAF5, Heart development, Craniofacial development, Metabolism

INTRODUCTION

Birth defects are a major cause of morbidity and mortality worldwide. Between 3-5% of live born infants have birth

defects including cardiac, craniofacial, and neurodevelopmental abnormalities that each contribute to adverse perinatal outcomes (Webber et al., 2015). While significant progress has been made identifying environmental contributors to birth defects, our understanding of their genetic basis remains incomplete (Kirby, 2017).


Transcriptional dysregulation represents an important mechanism leading to birth defects (Prescott and Wilkie, 2007). Gene regulatory networks that establish cell states, pattern tissues, and regulate cell differentiation and organ maturation are controlled by thousands of transcription factors, cofactors, and chromatin regulators. Failure to regulate these programs leads to a diverse array of developmental syndromes, including but not limited to, growth and intellectual disability, limb deformities, craniofacial anomalies, and congenital heart defects (Jenkins et al., 2007; de Soysa et al., 2019). It is increasingly recognized that pathogenic variants in key transcription factors are responsible for many developmental syndromes. These ‘general regulator’ transcription factors control gene expression and chromatin accessibility through selective recruitment of RNA Polymerase II and epigenetic machinery to specific genomic loci (Clark et al., 2006; Chen et al., 2022).

Recently, pathogenic variants in TATA Binding Protein Associated Factors (TAFs) key components of transcription factor TFIID have been identified in a subset of patients with intellectual disability, craniofacial hypoplasia, and congenital heart disease (O’Rawe et al., 2015). This syndrome has been termed as a ‘TAFopathy’ and includes mutations in TATA Binding Protein (*TBP*), *TAF1*, *TAF2*, *TAF6*, *TAF8*, and *TAF13* (Rooms et al., 2006; Tawamie et al., 2017; Hellman-Aharony et al., 2013; Alazami et al., 2015). The underlying mechanism by which TAFopathies give rise to neurodevelopmental, craniofacial, and cardiac abnormalities is not understood.

TFIID is a large complex comprised of multiple proteins including TBP and multiple TAFs. The complete TFIID complex and holo-TFIID (lacking TBP) bind to distinct DNA sequences (Wu and Chiang, 2001). Previous studies have identified specific DNA sequences to which TAFs bind within initiator and downstream promoter elements (Juven-Gershon et al., 2006; Juven-Gershon and Kadonaga, 2010). TAFs also interact with enhancers through bromodomain motifs (Lehmann et al., 2012). TAF1 and TAF5 are core components of TFIID complexes. TAF1 binds to DNA and TBP, forming a complex that recruits RNA Polymerase II at sites of transcription. TAF5 acts as a scaffold protein important for the assembly of TFIID components (Bieniossek et al., 2013; Wang et al., 2014). Further adding to the complexity, distinct TFIID complexes consisting of unique TAF combinations may mediate the effect of different

¹Center for Cardiovascular Research, Division of Cardiology, Department of Medicine, Washington University School of Medicine, St. Louis, MO 63110, USA. ²Departments of Nutritional Sciences, Dell Pediatrics Research Institute, University of Texas at Austin, Austin, TX 78723, USA. ³Departments of Neuroscience and Cell Biology, Washington University Center for Cellular Imaging, Washington University School of Medicine, St. Louis, MO 63110, USA. ⁴Department of Developmental Biology, Washington University School of Medicine, St. Louis, MO 63110, USA. ⁵Division of Oncology, Department of Medicine, Washington University School of Medicine, St. Louis, MO 63110, USA. ⁶Department of Immunology and Pathology, Washington University School of Medicine, St. Louis, MO 63110, USA.

*Author for correspondence (klavine@wustl.edu)

 R.G., 0000-0001-9668-6497; C.K., 0000-0003-3122-1677; K.J.L., 0000-0003-1948-9945

This is an Open Access article distributed under the terms of the Creative Commons Attribution License (<https://creativecommons.org/licenses/by/4.0>), which permits unrestricted use, distribution and reproduction in any medium provided that the original work is properly attributed.

transcriptional activators (Brou et al., 1993; Asturias, 2009; Louder et al., 2016).

Here, we report a novel zebrafish model of TAFopathies caused by nonsense mutations in *taf5*. *taf5*^{-/-} zebrafish display reduced survival, heart failure, and facial and cardiac hypoplasia and fail to thrive. These findings were recapitulated in *taf1*^{-/-} zebrafish. Mechanistically, we reveal roles for TAF1 and TAF5 in coordinating metabolic programs essential for craniofacial and cardiac development.

RESULTS

cora^{stl325/stl325} embryos show signs of early-onset heart failure

We recovered a mutation from an ENU mutagenesis screen that displayed a small heart and craniofacial hypoplasia and lethality, which we referred to as *corazoncito*^{stl325} (*cora*^{stl325}) (Gray et al., 2021). Affected embryos demonstrate evidence of heart failure in Mendelian ratios suggestive of a recessive allele (Fig. 1A). To characterize the cardiac phenotype in detail, we first observed the temporal progression of heart failure in progeny obtained from a *cora*^{stl325/+} carrier self-cross. *cora*^{stl325/stl325} embryos displayed a collapsed heart and pericardial edema beginning at 96 h post-fertilization (hpf). *cora*^{stl325/stl325} hearts were visually indistinguishable from unaffected clutch mates at 72 hpf (Fig. 1A). We observed 100% mortality of embryos that displayed the *corazoncito* phenotype within 2 weeks post-fertilization (Fig. 1B). Quantitatively, *cora*^{stl325/stl325} embryos had a nearly three-fold increase in pericardial surface area compared to unaffected clutch mates (Fig. 1C). Measurement of ejection fraction by bright field imaging indicated that *corazoncito* embryos displayed evidence of systolic ventricular dysfunction (Fig. 1D).

To further characterize defects in cardiac function, we crossed *cora*^{stl325/+} to the cardiomyocyte-specific fluorescent reporter, *Tg(cmlc2: GFP)* (Huang et al., 2003). Lightsheet microscopy performed at 96 hpf confirmed reduced ejection fraction in *corazoncito* embryos (Fig. 1E,F; Movies 1,2). Lightsheet microscopy afforded us sufficient resolution to visualize changes in wall thickness and cellular dimensions throughout the cardiac cycle. This technique revealed that *cora*^{stl325/stl325} embryos displayed significant decreases in systolic wall thickening, longitudinal, and radial strain. Measurement of cardiomyocyte dimensions throughout the cardiac cycle indicated that *cora*^{stl325/stl325} cardiomyocytes failed to shorten and thicken in systole suggestive of systolic dysfunction. Furthermore, we observed that *cora*^{stl325/stl325} cardiomyocytes were shorter and thicker in diastole compared to controls indicative of concomitant diastolic dysfunction (Fig. 1F).

cora^{stl325/stl325} hearts show normal atrial and ventricular architecture, chamber patterning, and sarcomere formation (Fig. 2A, B). Serial imaging of *cora*^{stl325/stl325} *Tg(cmlc2:GFP)* hearts revealed diminished ventricular area compared to clutch mates beginning at 72 hpf. Atrial area did not differ between experimental groups (Fig. 2C,D). Measurement of bromodeoxyuridine (BrdU) incorporation – a synthetic nucleoside analogue used to study cell proliferation in living tissues – showed reduced abundance of replicating myocardial cells in *cora*^{stl325/stl325} embryos compared to unaffected siblings. We did not observe differences in abundance of replicating pericardial cells as indicated by the number of BrdU positive cells present in the pericardium (Fig. 2E). Together, these data support the hypothesis that *cora*^{stl325/stl325} embryos show signs of embryonic heart failure and ventricular hypoplasia.

cora^{stl325/stl325} embryos have craniofacial deformities and neuroanatomical defects

In addition to cardiac defects, we observed evidence of craniofacial hypoplasia in *cora*^{stl325/stl325} embryos (Fig. 3A). At 96 hpf, *corazoncito* mutants displayed a 33% reduction in head-to-body and eye-to-body ratios despite slight reductions in body length seen in *cora*^{stl325/stl325} embryos (Fig. 3B). We performed Alcian Blue staining to evaluate cartilaginous structures, which revealed hypoplastic jaw cartilage (Meckel's Cartilage, Ethmoid plate, Trabecula) in *cora*^{stl325/stl325} embryos (Fig. 3C). Histology of 96 hpf sections suggest that chondrocytes that were specified appear morphologically similar between *cora* and wild-type clutchmates (Fig. 3D). Imaging of *Tg(crestin::GFP)* (migratory neural crest cell marker) and *Tg(sox10::RFP)* (cartilage progenitor marker) embryos demonstrated evidence of delayed neural crest cell migration and cartilage specification in *cora*^{stl325/stl325} embryos (Fig. 3E) (Kaufman et al., 2016). X-ray microscopy further demonstrated reduced brain volume in *cora*^{stl325/stl325} embryos compared to unaffected siblings (Fig. 3F). Together, these data indicate that *cora*^{stl325/stl325} embryos display impaired craniofacial and neurodevelopment.

cora^{stl325/stl325} is a nonsense mutation in *taf5*

To map the *cora*^{stl325/stl325} mutation, we crossed *cora*^{stl325/stl325} carriers (SAT background) into the SJD mapping background as described in Gray et al. (2021) (Kaufman et al., 2016). *cora*^{stl325/stl325}/SJD F1 carriers were identified and self-crossed. F2 embryos were collected, pooled into *cora*^{stl325/stl325} and unaffected clutch mate groups, genomic DNA isolated, and whole genome sequencing performed (Fig. 4A). We identified an area on Chromosome 1 that retained homozygosity for the AB* background that was found exclusively in embryos displaying the *cora*^{stl325/stl325} phenotype (Fig. 4B). Fine chromosomal mapping identified a region on Chromosome 1 (24cM) that was closely linked with the *corazoncito* phenotype (Fig. 4C). By curating mutations found in the mapped region, we discovered a nonsense mutation in exon 3 of *taf5* (Fig. 4D). We developed a genotyping assay that specifically targeted the mutant base-pair substitution by HpyCH4III restriction digest. Genotyping of 49 embryos demonstrated 100% association between the mutated base pair and *corazoncito* phenotype, although Sanger sequencing of individual mutant embryos has not been performed (Fig. 4C).

To rigorously implicate *taf5* loss of function as the cause of the *corazoncito* phenotype, we generated a stable *taf5* null allele using CRISPR/Cas9-mediated mutagenesis (referred to as *taf5*^{stl852}). *taf5*^{stl852/stl852} embryos recapitulated the *corazoncito* phenotype of heart failure and craniofacial hypoplasia. Furthermore, *cora*^{stl325} failed to complement the *taf5*^{stl852} allele (Fig. 5A). Quantitative measurements of pericardial edema, ejection fraction, head-to-body, and eye-to-body ratio were consistent across *cora*^{stl325/stl325}, *taf5*^{stl852/stl852}, and *cora*^{stl325}/*taf5*^{stl852} groups (Fig. 5B,C). Measurement of *taf5* mRNA expression by quantitative RT-PCR revealed marked reductions in *taf5* expression in *cora*^{stl325/stl325}, *taf5*^{stl852/stl852}, and *cora*^{stl325}/*taf5*^{stl852} embryos compared to controls (Fig. 5E). WISH further revealed that *taf5* was expressed in the whole head and whole heart region. No *taf5* mRNA was detected in *cora*^{stl325/stl325} or *taf5*^{stl852/stl852} embryos (Fig. 5F). Collectively, these findings support the conclusion that *taf5* loss of function is responsible for the *corazoncito* phenotype.

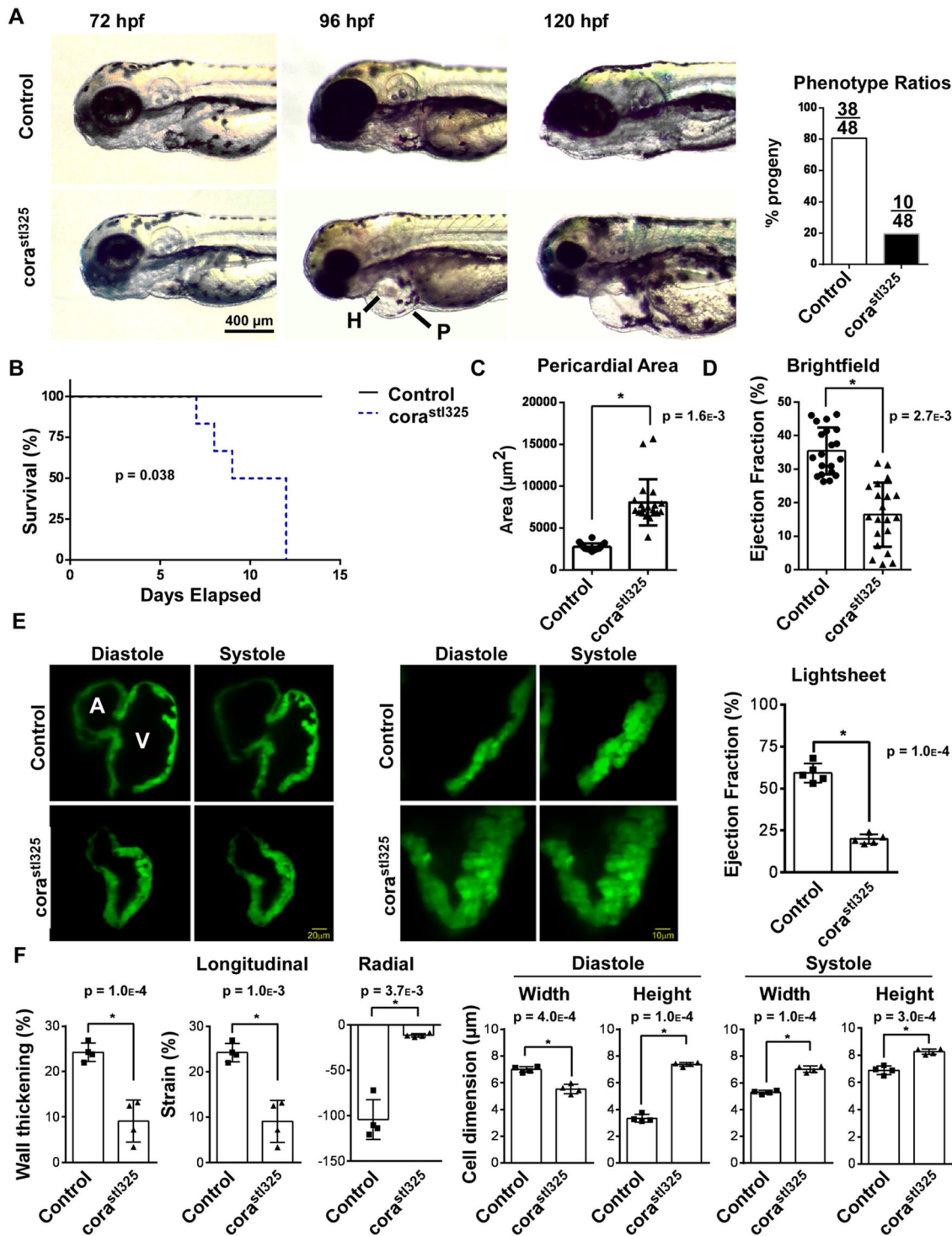


Fig. 1. *corast^{1325/st1325}* embryos display reduced survival and heart failure. (A) Light microscopy showing the emergence of pericardial edema between 72 and 120 h post fertilization (hpf). P, pericardium; H, heart. Phenotype ratios are presented on the right. (number of trials=4; number of samples per trial=48) (B) Survival curve of *cora^{st1325}* embryos relative to their unaffected clutchmates (number of trials=4; number of samples per trial=48). (C) Quantification of light microscopy images measuring area of the pericardium (number of trials=4; number of samples per trial=48). (D) Quantification of light microscopy images measuring ejection fraction (number of trials=4; number of samples per trial=48). (E) Lightsheet microscopy generated images of 96 hpf embryos harboring the *cmc1::GFP* transgenic reporter. Hearts are shown in systole and diastole. A, atrium; V, ventricle. Quantification of ejection fraction ($n=4$). (F) Quantification of changes in cell dimension using lightsheet-generated videos ($n=4$).

***taf1* deletion recapitulates the *corazoncito* phenotype**

TAF5 acts as a scaffold protein important for the assembly of TFIID components (Bieniossek et al., 2013). Coincidentally, studies on TAF1, the catalytic subunit of TFIID, have shown that

knockdown of TAF1 results in a similar phenotype of aberrant neurodevelopment (Jacobson et al., 2000). To directly compare phenotypes elicited by deletion of *taf5* and *taf1*, we utilized Cas9/CRISPR gene editing to generate a new null allele of *taf1* (referred

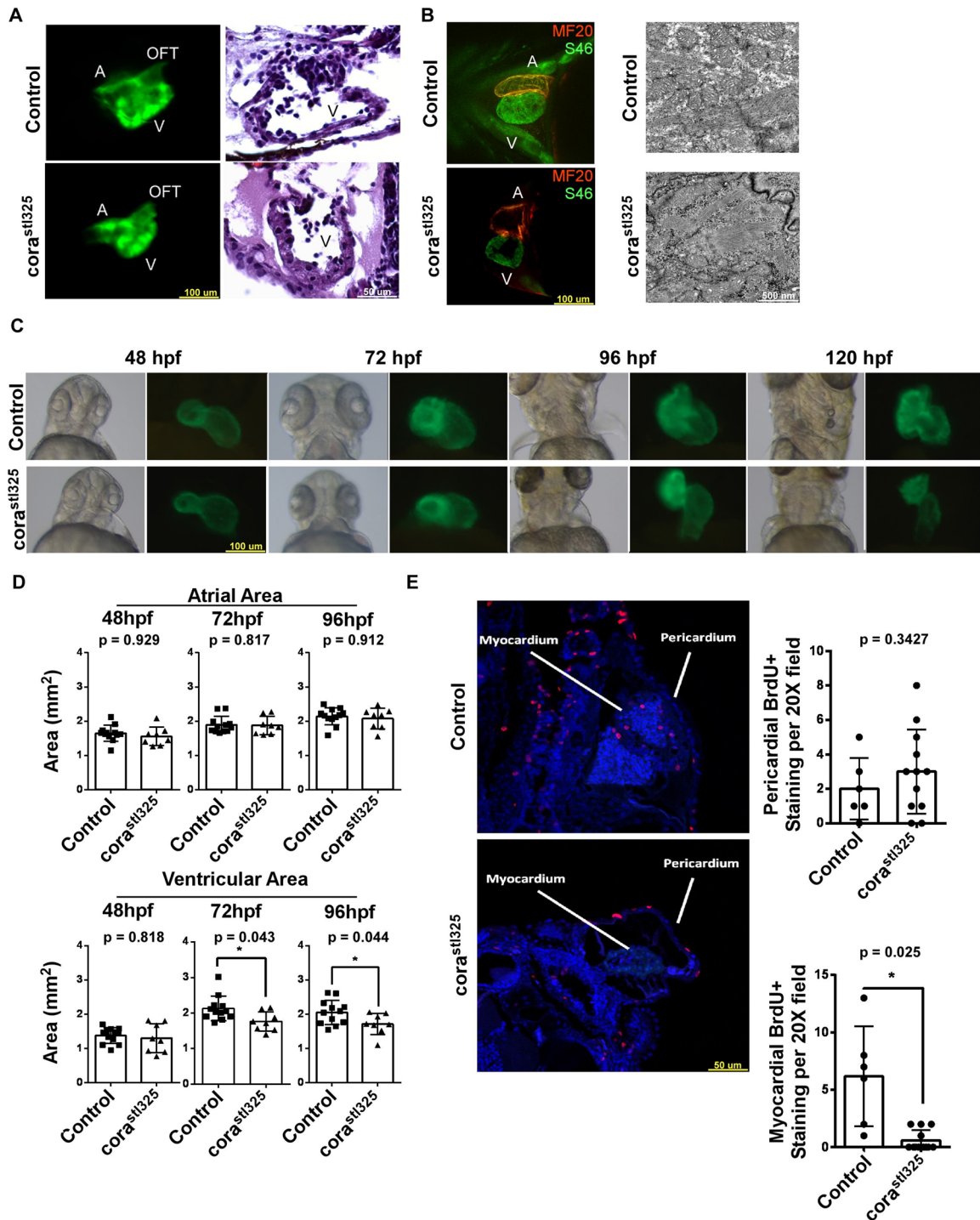


Fig. 2. *cora^{stl325}* hearts display hypoplasia and reduced proliferation. (A) Fluorescent microscopy images of 96 hpf embryos (left, *cmlc2::GFP*; $n=8$) and H&E staining (right; $n=4$). (B) Fluorescent microscopy images of 96 hpf embryos stained with the SF46 (orange) and MF20 (green) showing normal atrioventricular patterning (left). Electron microscopy showing intact sarcomeres in control and *cora^{stl325}* cardiomyocytes (right; $n=4$). (C) Brightfield and fluorescence microscopy time-course of *cmlc2::GFP* expression between 48 and 120 hpf (Control ($n=12$) and *cora^{stl325}* ($n=8$)). (D) Quantification of atrial and ventricular cross-sectional areas obtained from C [Control ($n=12$) and *cora^{stl325}* ($n=8$)]. (E) BrdU immunostaining (red) of 96 hpf embryos embedded in paraffin [Control ($n=6$) and *cora^{stl325}* ($n=12$)].

to as *taf1^{stl456/stl456}*). We observed evidence of pericardial edema, reduced ejection fraction, and craniofacial hypoplasia in *taf1^{stl456/stl456}* mutant embryos relative to unaffected siblings. Consistent with these phenotypes *taf1* mRNA was expressed in the head and heart regions at 96 hpf (Fig. 6A-D). Alcian Blue staining demonstrated severe hypoplasia and loss of craniofacial

cartilaginous structures (Fig. 6E), whereas X-ray microscopy showed reduced brain volume (Fig. 6F). We next performed whole mount *in situ* hybridization for markers of craniofacial development and brain patterning. WISH indicated that *crestin* expression was similar between control and *taf1^{stl456/stl456}* embryos, suggesting that neural crest cells specification is not

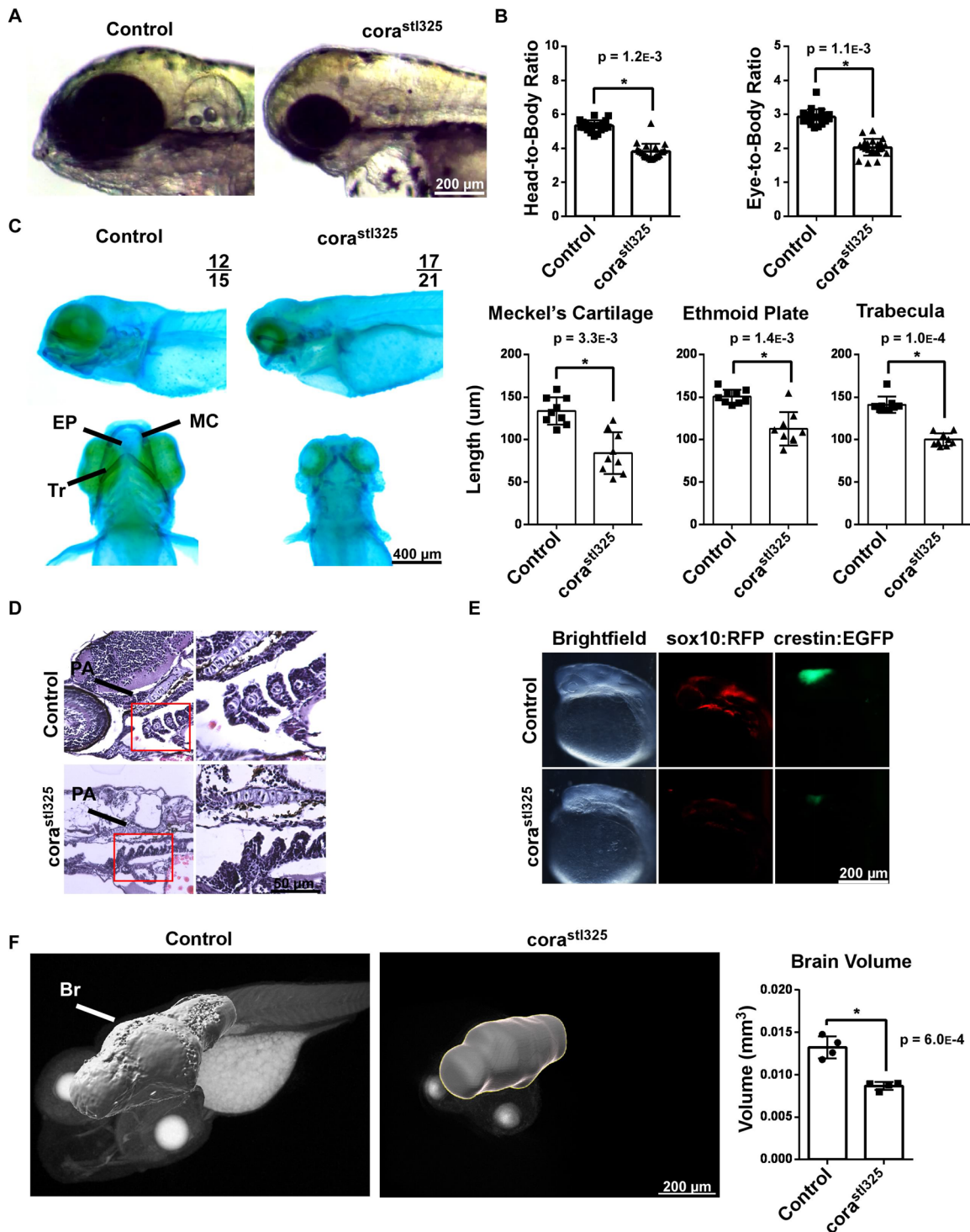


Fig. 3. *cora^{stl325}* embryos have craniofacial deformities and neuroanatomical defects. (A) Head morphology of control and *cora^{stl325}* embryos at 96 hpf. (B) Head-to-body and head-to-eye ratios. Control ($n=13$), *cora^{stl325}* ($n=9$). (C) Alcian Blue staining of control and *cora^{stl325}* embryos at 96 hpf (left), with quantification of major jaw elements (right). EP, Ethmoid plate; MC, Meckel's Cartilage; T, Trabeculae. $n=9$ per experimental group. (D) H&E staining of the jaw of control and *cora^{stl325}* embryos at 96 hpf. (E) Fluorescence microscopy images of Tg(crestin::GFP) and Tg(sox10::RFP) control and *cora^{stl325}* embryos. (F) X-ray microscopy-generated images of 96 hpf embryos (left) and quantification of tissue volume (right). Br, brain Control ($n=4$), *cora^{stl325}* ($n=4$).

impacted by *tafl* inactivation. In contrast, *sox10* expression was markedly reduced indicating a defect in the differentiation of cartilage progenitors from neural crest cells (Fig. 6G). We also observed decreased expression of pan-neural (*neurog1*), forebrain (*six3b*), and midbrain (*adcyp1b*) markers and an expansion of the

hindbrain marker, *zic2a* (Fig. 6H). Collectively, these findings indicate an overlapping phenotype between *tafl* and *taf5* mutant embryos that recapitulates key features of TAFopathies. The phenotype of *tafl* mutant embryos was comparable to that of *taf5* mutant embryos.

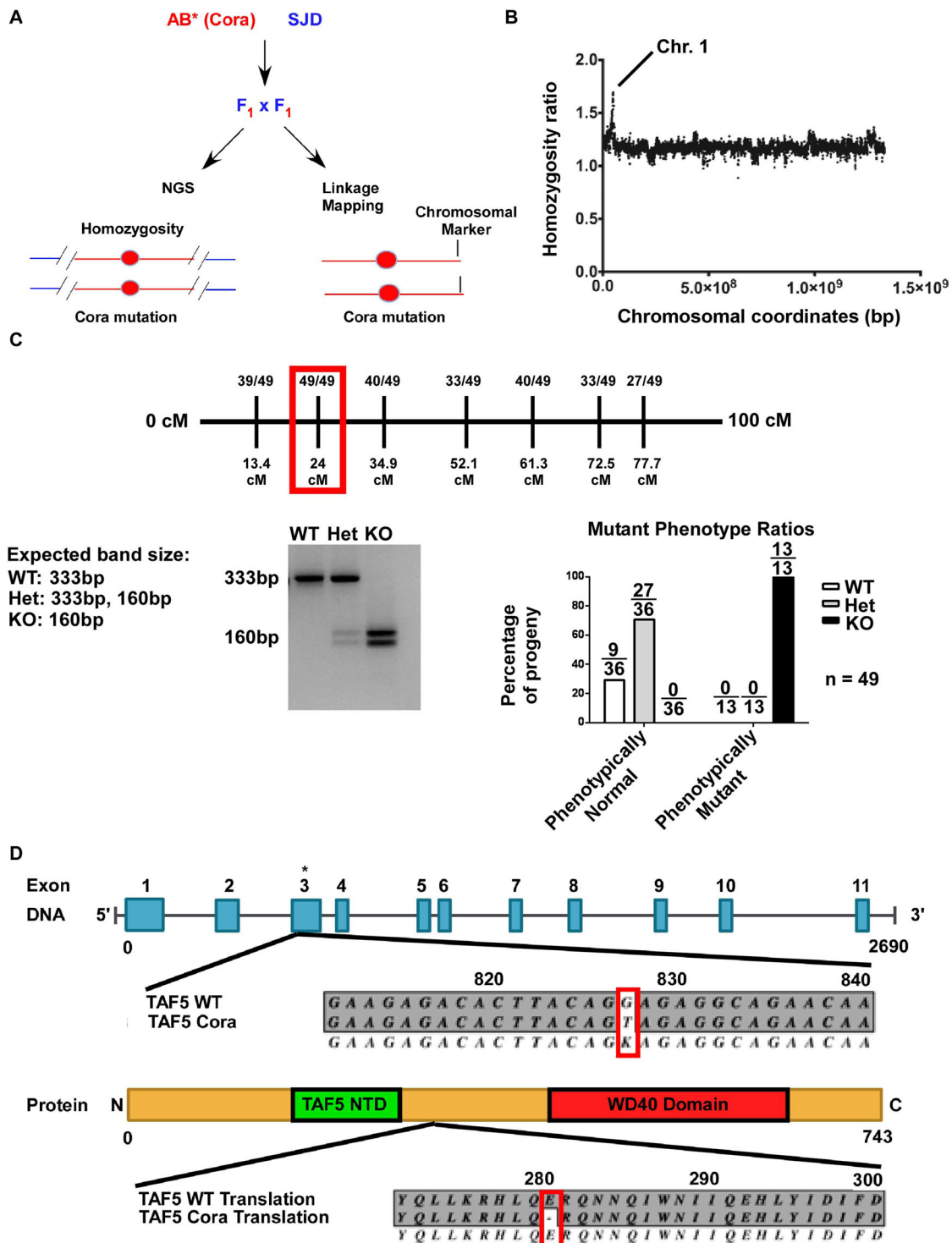


Fig. 4. *cora^{stl325}* encodes a nonsense mutation in *taf5*. (A) Workflow for mapping *cora^{stl325}* using whole genome next generation sequencing. (B) Manhattan plot displaying homozygosity ratio for the AB* background (y-axis) as a function of chromosome location (x-axis). A value of 2.0 indicates 100% homozygosity for the AB* background. Chr. 1: chromosome 1. (C) Fine chromosomal mapping identified a 24 cM region (red box) that was linked with the *cora^{stl325}* phenotype (top). Genotyping to identify the point mutation leading to a nonsense mutation in *taf5*. The nonsense mutation was linked to the *cora^{stl325}* phenotype (bottom). (D) Graphical representation of the *taf5* genomic locus and TAF5 protein including major functional domains. Red box indicates the mutated base and resulting nonsense mutation.

taf5 is dispensable for embryonic development

taf5 is closely related (46% amino acid identity) to an evolutionarily conserved homolog, *taf5l* (Fig. S1A). To ascertain its function and examine potential redundancy between *taf5* and *taf5l*, we generated

a null allele in exon 2 of *taf5l*, *taf5l^{stl851}*, WISH revealed that *taf5l* was expressed ubiquitously throughout WT embryos, whereas *taf5l* RNA was not detected in embryos homozygous for our nonsense allele (Fig. S1B). *taf5l^{stl851/stl851}* mutant embryos were viable and

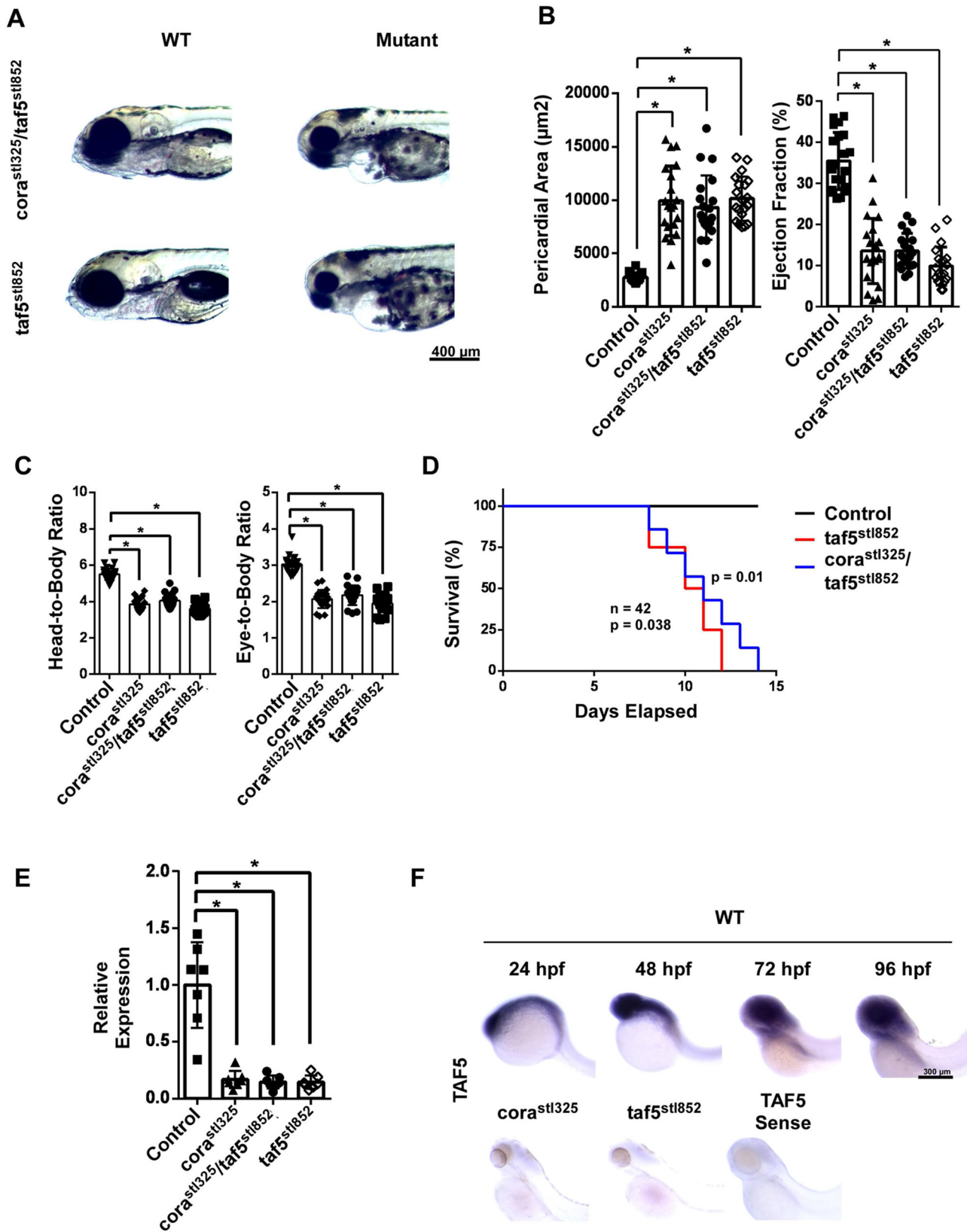


Fig. 5. *cora^{stl325}* is a null allele of *taf5*. (A) Brightfield images of control, *cora^{stl325}*, *taf5^{stl852}*, and *cora^{stl325}/taf5^{stl852}* embryos at 96 hpf. (B) Measurement of pericardial area and ejection fraction in control, *cora^{stl325}*, *taf5^{stl852}*, and *cora^{stl325}/taf5^{stl852}* embryos at 96 hpf. *n*=22. (C) Measurement of head-to-body and head-to-eye ratios in control, *cora^{stl325}*, *taf5^{stl852}*, and *cora^{stl325}/taf5^{stl852}* embryos at 96 hpf. *n*=22. (D) Survival of control, *taf5^{stl852}*, and *cora^{stl325}/taf5^{stl852}* CRISPR embryos. *n*=42. (E) RTPCR for *taf5* mRNA in control, *cora^{stl325}*, *taf5^{stl852}*, and *cora^{stl325}/taf5^{stl852}* embryos at 96 hpf. *n*=7. (F) Time course of *taf5* mRNA expression by whole-mount *in situ* hybridization (top) and *taf5* mRNA expression in *cora^{stl325}* and *taf5^{stl852}* embryos at 96 hpf. Note: all brackets marked with ** represent *P*<1E-4.

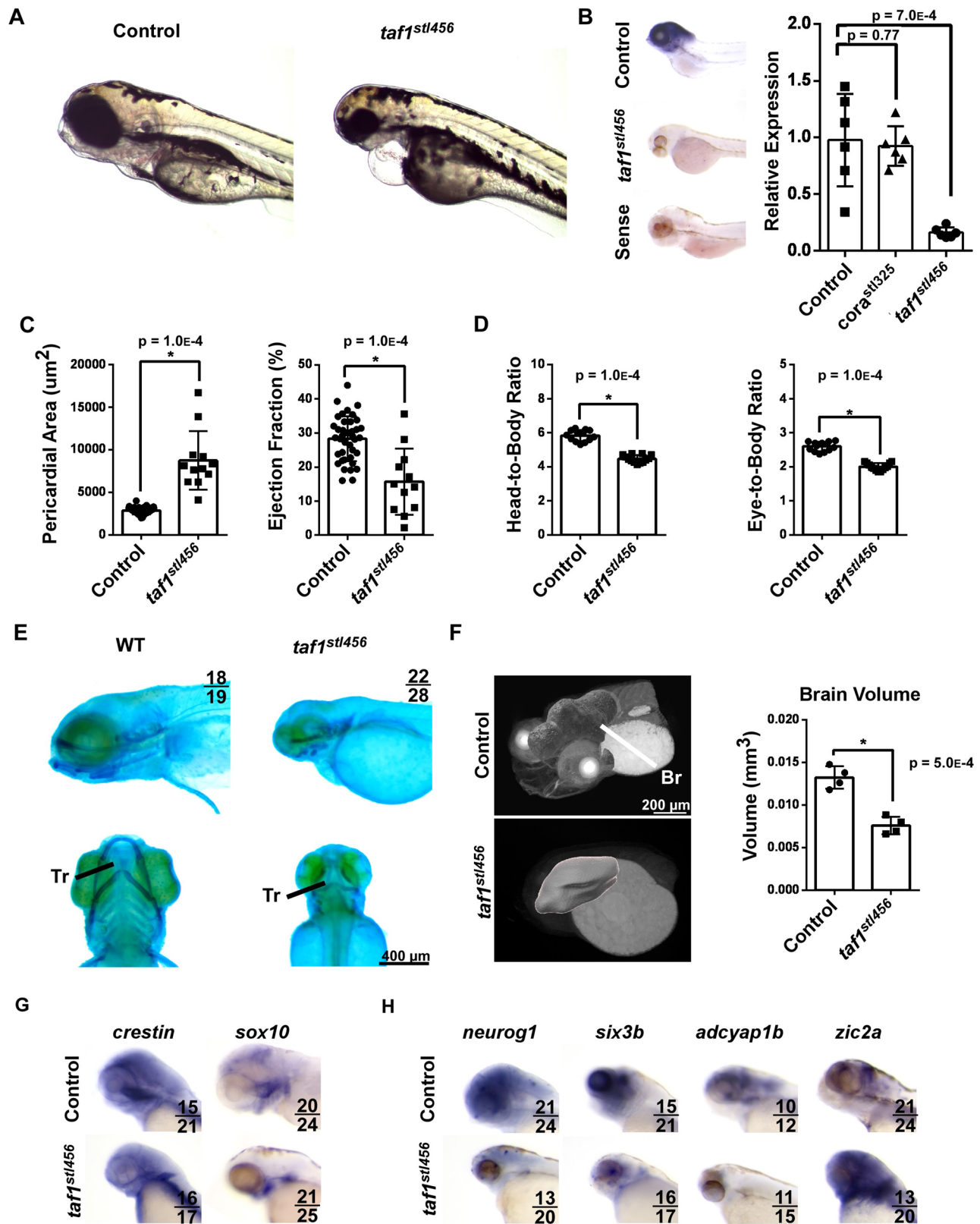


Fig. 6. *taf1* deletion recapitulates the corazoncito phenotype. (A) Brightfield images of control and *taf1^{stl456/stl456}* embryos at 96 hpf. (B) *taf1* mRNA expression measured by *in situ* hybridization (left) and RT-PCR (right). $N=6$ per experimental group. (C) Quantification of pericardial area (left) and ejection fraction (right) in control ($n=30$) and *taf1^{stl456/stl456}* ($n=12$) embryos at 96 hpf. (D) Quantification of head-to-body ratio (left) and head-to-eye ratio (right) in control ($n=21$) and *taf1^{stl456/stl456}* ($n=20$) embryos at 96 hpf. (E) Alcian Blue staining of control and *taf1* knockout (KO) embryos. (F) X-ray microscopy-generated images of control and *taf1* KO embryos at 96 hpf (left). Quantification of brain volume (right). $N=4$ per experimental group. Br, brain (red), heart (blue). (G) Whole-mount *in situ* hybridization of *crestin* and *sox10* mRNA expression in control and *taf1* KO embryos at 96 hpf. (H) Whole-mount *in situ* hybridization of neuronal (*neurog1*) and brain region markers (*six3b*, *Adcyap1b*, *zic2a*).

did not display any evidence of craniofacial hypoplasia, pericardial edema, or reduced cardiac function at 96 hpf and grew into fertile adults. Crosses of *taf5^{stl851/stl851}* fish to test for possible maternal effects produced normal progeny, indicating that *taf5* is dispensable for development. Furthermore, compound mutant analyses indicated that loss of *taf5* function did not worsen craniofacial and cardiac phenotypes observed in *taf5* mutant (*corazoncito*) embryos (Fig. S1C,D) suggesting that *taf5* and *taf5l* are not redundant.

***taf5* regulates oxidative metabolism**

As *taf5* is a member of the TFIID complex (Patel et al., 2018) and likely regulates transcription, we performed RNAseq to investigate potential mechanisms by which *taf5* loss of function contributes to the observed cardiac phenotypes. We isolated RNA from embryonic hearts recovered from *cora^{stl325/stl325}*; *Tg(cmlc2::gfp)* embryos and their unaffected *Tg(cmlc2::gfp)* clutchmates at 96 hpf. Control and *cora^{stl325/stl325}* sequencing libraries were generated from pooled samples each containing 100 hearts. Principal component analysis (PCA) revealed markedly distinct transcriptional profiles between control and *cora^{stl325/stl325}* hearts, with 2274 genes showing a log₂ fold value of 1 or greater in expression (Fig. 7A). Pathway analysis suggested alterations in several distinct biological processes including metabolism (Fig. 7B). *cora^{stl325/stl325}* hearts displayed downregulation of numerous genes involved in the TCA cycle (9/17 genes) and the Electron Transport Chain (56/118 genes) (Fig. 7C,D). Interestingly, other major pathways, including glycolysis (7/20), amino acid (10/24), and lipid (20/26) metabolism were significantly impacted.

To determine whether metabolic genes were globally downregulated, we collected RNA from control, *cora^{stl325/stl325}*, and *taf1^{stl456/stl456}* whole embryos at 96 hpf. Quantitative RT-PCR confirmed reduced *aspdh*, *suclg2*, *aidm5*, and *cox4il* mRNA expression in *cora^{stl325/stl325}* and *taf1^{stl456/stl456}* embryos relative to unaffected siblings (Fig. 8A). To discern whether altered metabolic gene expression affected metabolic function, we measured whole embryo basal metabolic rate using a Seahorse XF24 Bioanalyzer at 96 hpf. These studies showed diminished oxygen consumption rate (OCR) in *cora^{stl325/stl325}* and *taf1^{stl456/stl456}* embryos relative to control clutch mates. To verify that decreased basal metabolic rate was not a secondary result of heart failure, we measured basal OCR in embryos lacking *ttna* (*ttna^{stl853}*), an established model of profound heart failure (Fig. S2) (Nechiporuk et al., 1999). Basal OCR did not differ between control and *ttna^{stl853/stl853}* embryos (Fig. 8B). Reduced metabolic activity was further supported by increased NAD/NADH and ADP/ATP ratios in *cora^{stl325/stl325}* and *taf1^{stl456/stl456}* embryos relative to control siblings and *N2:ttna* embryos (Fig. 8C). Mitochondrial function was assessed using an Oroboros O2k-FluoRespirometer at 96 hpf. Consistent with the Seahorse data, *cora^{stl325/stl325}* mitochondrial respiration showed significant perturbations at all states of respiration (Fig. 8D). Together, these results suggest that *taf1* and *taf5* are essential regulators of oxidative metabolism during embryonic development.

DISCUSSION

While the biochemical properties of TAFs and the TFIID complex are well understood, much remains to be learned regarding their *in vivo* functions, including roles during embryonic development and tissue homeostasis as well as how pathogenic variants in TAFs contribute to diseases. Here, we leveraged several genetic zebrafish models we generated to identify a causal link between mutations in *taf1* and *taf5*, TAFopathy phenotypes, and derangements in

metabolism. These studies suggest that the TAF complex does not only globally regulate transcription, but rather acts as a selective modulator of specific transcriptional programs. Furthermore, our findings provide new insights implicating defects in metabolism in the pathogenesis of TAFopathies.

TAFs are general transcription factors that are TFIID complex components which recruit RNA polymerase II to gene promoters to form the pre-initiation complex (PIC) (Patel et al., 2018). Many TAFs modulate interactions between gene-specific transcriptional activators and general transcription machinery by either stabilizing or inducing conformation changes to the PIC (Zou et al., 2015; Rhee and Pugh, 2012). Structurally, TAF5 forms a homodimer and acts as a scaffold for TFIID complex formation. Its C-terminus contains a WD40 domain, which mediates protein-protein interactions and may be important for TAF-TAF interactions (Roeder, 1996). TAF1 is the largest subunit of TFIID and contains multiple domains with enzymatic activity and chromatin interaction capabilities (Oelgeschläger et al., 1998; Wang et al., 2014). Recent studies have revealed that the TFIID complex is a three-lobed, asymmetric structure and that the TAF1 and TAF5 subunits contribute to forming this characteristic structure (Bhattacharya et al., 2007; Oelgeschläger et al., 1998).

The alleles generated in this study for *taf5*, *taf5l*, and *taf1* all contained nonsense mutations that represent loss of function phenotypes. Interestingly, while it is believed that *taf5* and *taf1* operate in the same complex, deletion of one did not impact the expression of the others. Phenotypically, we show that *taf5* and *taf1* are necessary for embryonic heart, craniofacial, and brain development in zebrafish. Brightfield and fluorescent microscopy revealed classical signs of heart failure in *taf5* and *taf1* mutant (loss of function, null alleles) as measured by reduced ejection fraction, dimensional cardiomyocyte strain, and pericardial edema. Despite these functional defects, neither *taf5* nor *taf1* were necessary for heart patterning, as atrioventricular staining revealed no obvious differences in chamber specification or structural architecture. Instead, we observed decreased myocardial proliferation in *taf5* mutants. Proliferation of other structures such as the pericardium was not affected, suggesting a cell-specific role for *taf5* in myocardial proliferation. Consistent with this finding, TAF1 upregulates cyclin D and cyclin A expression through TAF1 histone acetyltransferase activity (Jacobson et al., 2000) and TAF1 has been shown to associate with the leukemia-promoting oncogene AML1-ETO, which promotes proliferation of AML1-ETO-expressing myeloid leukemia cells. Furthermore, TAF1 is required for leukemic cell self-renewal, and its reduction promotes the differentiation and apoptosis of AML1-ETO+ myeloid leukemia cells (Gangloff et al., 2000).

We also observed significant decreases in head size, brain volume, and disruption of defined brain regions in *taf5* and *taf1* mutants. Neurodevelopmental defects have been previously observed in *taf1* mutants as evidenced by decreased head-to-body and eye-to-body ratios, and measurements of optic tectum size (Kloet et al., 2012). Loss of TAF1 in rats alters the morphology and function of the cerebellum and cerebral cortex, and leads to hypoplasia and loss of Purkinje cells, with behavioral abnormalities paralleling that seen in TAF1/MRSX33 intellectual disability syndrome (Xu et al., 2019). TAF1 has also been linked to X-linked dystonia parkinsonism, with an alternatively spliced transcript of TAF1 discovered in neurons (Gudmundsson et al., 2019; Grune et al., 2022; Capponi et al., 2021). These findings implicate TAF1 in early neurodevelopment and aging.

To illuminate mechanisms that contribute to TAFopathies in our zebrafish models, we performed RNA sequencing in *taf5* mutant

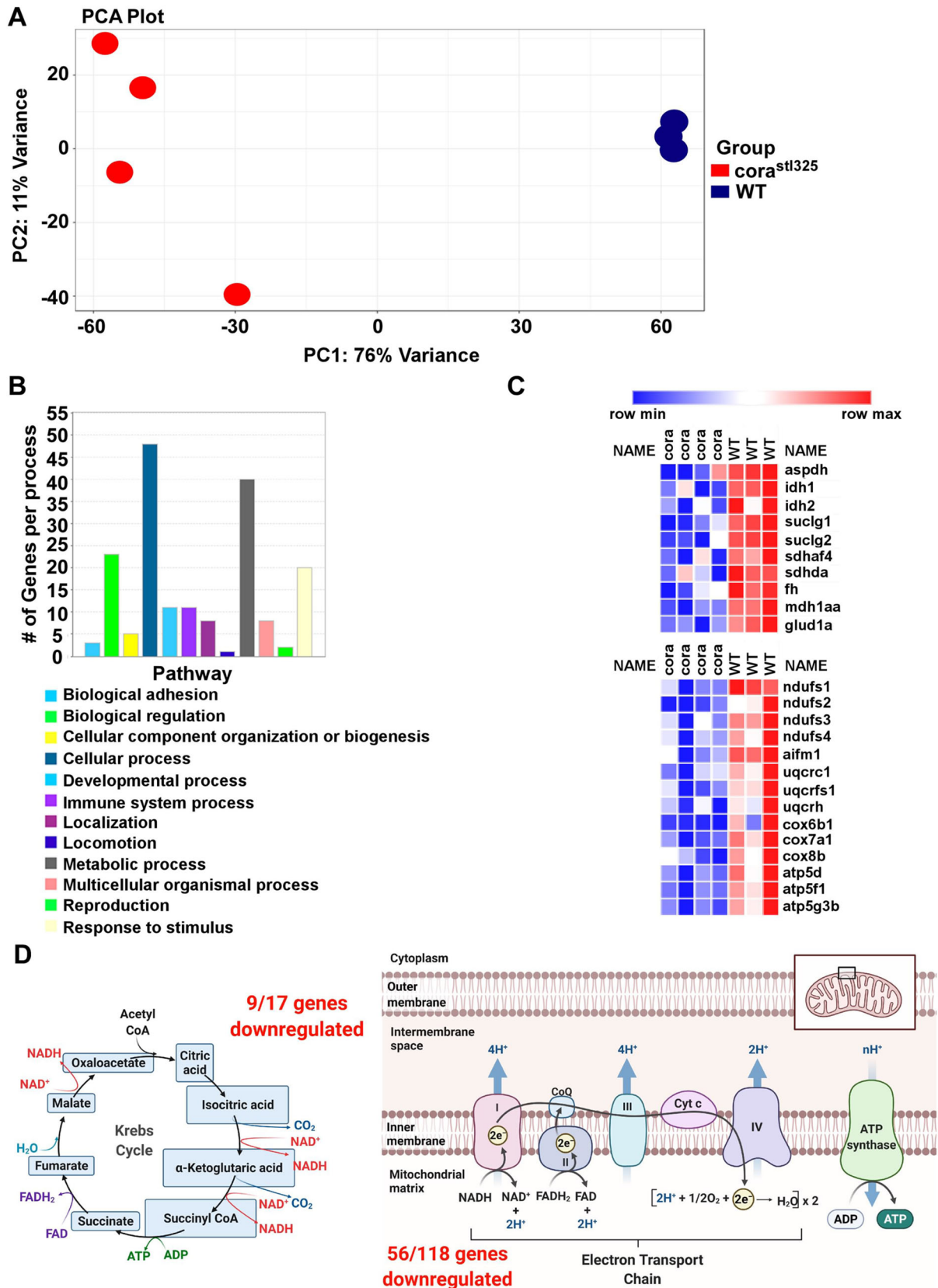


Fig. 7. RNA sequencing of control and *cora^{stl325}* identifies derangements metabolic gene expression. (A) Principal component analysis (PCA) plot of pooled sequencing libraries generated from control and *cora^{stl325}* embryos at 96 hpf. Each dot represents a pool of 100 embryonic hearts. (B) Bar graph of the top Gene Ontology (GO) pathways associated with genes differentially expressed between control and *cora^{stl325}* hearts. (C) Heat map of metabolic genes significant with significantly reduced expressed in *cora^{stl325}* hearts. (D) Graphical representation of the number of differentially expressed metabolic genes associated with the TCA cycle (left) and the electron transport chain (right). Made with BioRender.

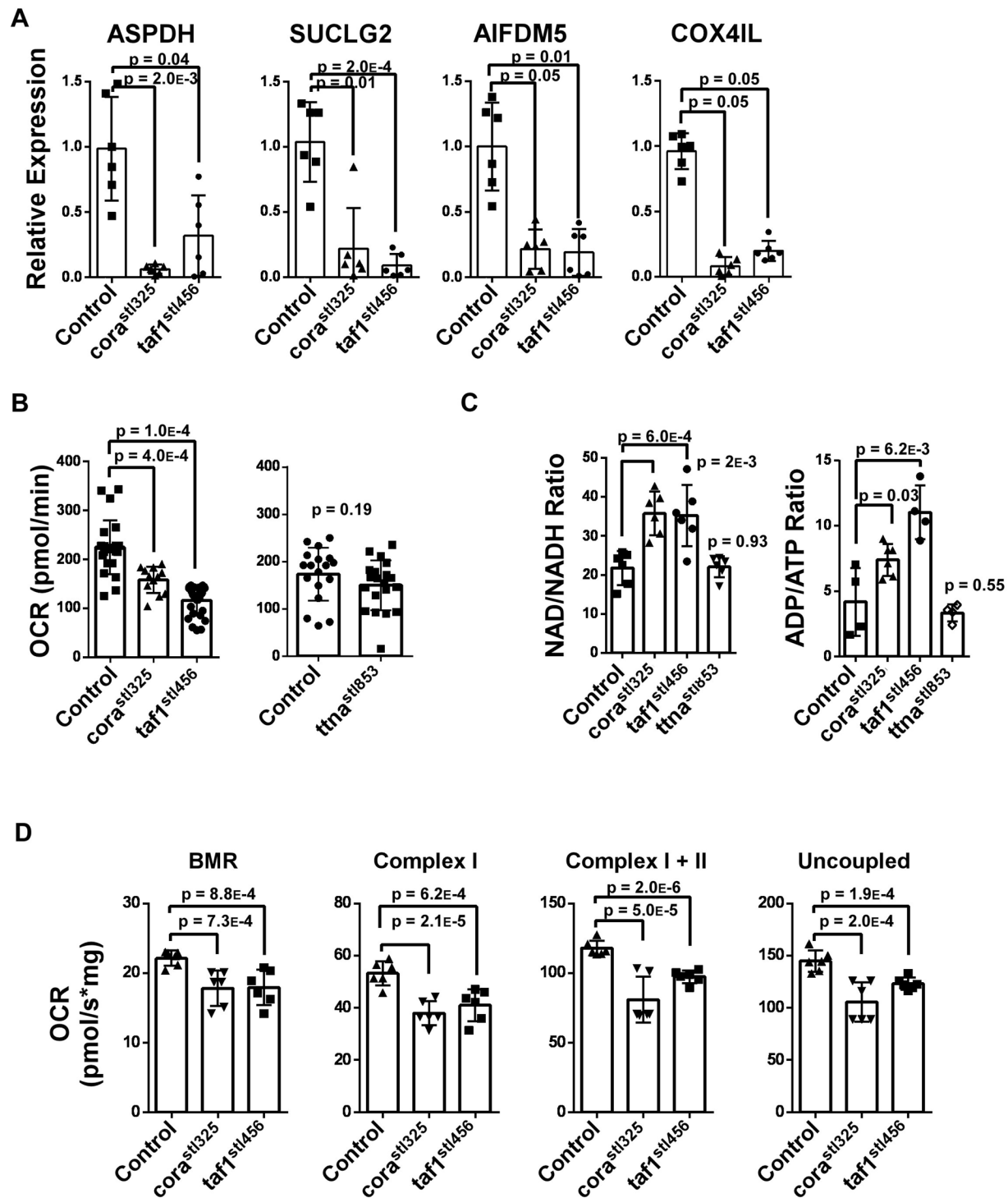


Fig. 8. Defective oxidative metabolism in *cora*^{sti325} and *taf1* knockout embryos. (A) RTPCR showing the reduced expression of genes involved in the TCA cycle (*Aspdh*, *Suclg2*) and the electron transport chain (*Aifdm5*, *Cox4il*) in *cora*^{sti325} and *taf1*^{sti456} embryos at 96 hpf. Each data point represents a pool of 20 embryos. (B) Reduced basal oxygen consumption rates (OCR) in *cora*^{sti325} ($n=12$) and *taf1*^{sti456} ($n=12$) embryos compared to controls at 96 hpf (left). Preserved basal OCR in *ttna*^{sti853/sti853} ($n=20$) compared to controls ($n=18$) embryos at 96 hpf (right). Data were obtained from a Seahorse XF24 Bioanalyzer. (C) Targeted metabolite assays measuring NAD/NADH (left) and ADP/ATP (right) in control, *cora*^{sti325} *taf1*^{sti456}, and *ttna*^{sti853/sti853} embryos at 96 hpf. $n=4$ pools of 100 embryos per genotype. (D) Oxygen consumption rates of isolated mitochondria for fatty acid metabolism. $n=4$ pools of 100 embryos per genotype

hearts. Surprisingly, we did not detect global downregulation of transcription. Instead, we identified specific reductions in the expression of genes involved in metabolism: fatty acid oxidation, TCA cycle, and electron transport chain. Derangements in metabolism were further supported by reduced expression of key

metabolic genes throughout the embryo, increased NAD/NADH and ADP/ATP ratios, and measurements of oxygen consumption at the organismal and mitochondrial levels. Importantly, these metabolic derangements were absent in *N2:TTNa* mutants with akinetic hearts indicating that metabolic impairments found in *taf1*

and *taf5* embryos were not secondary to heart failure. Indeed, metabolic remodeling plays an essential role in cardiac hypertrophy and heart failure (Al Ali et al., 2021; Aneichyk et al., 2018; Ashrafian et al., 2007). Consistent with previous findings in *taf1* mutants, we observed downregulation of the cell cycle regulator *cyclin D (ccnd1)* in *taf5* mutant hearts along with reduced expression of many other cyclins (*ccna1*, *ccna2*, *ccnb2*, *ccnb3*, *cne1*). Whether heart, craniofacial, and/or brain hypoplasia is primarily caused by metabolic remodeling or a direct effect on the transcription of cell cycle regulators represents an avenue for future investigation that will require dedicated tools that dissect the gene regulatory networks controlled by TAFs and the TFIIID complex.

Our study is not without limitations. We primarily focused on zebrafish models and validation of our findings pertaining to the phenotypic impact of *taf1* and *taf5* mutations and impact on metabolism in mammalian systems is an important next step. In support of our findings, previous studies have suggested that perturbations in zebrafish *taf1* result in overlapping phenotypes including reduced embryo length, underdeveloped cartilage, short pectoral fins, edema, and body axis deformations (Kloet et al., 2012). Our work adds to the understanding of the requirement for *taf1* during zebrafish development and provides new information implicating a similar requirement for *taf5* in craniofacial, neurodevelopmental, and cardiac development. The precise mechanism by which *taf1* and *taf5* specifically regulate transcriptional programs such as metabolism remains to be defined. An interesting possibility is that the TAF complex may optimize interactions between promoter and enhancer regions through the BRD complex, as TAF1 contains both TATA binding protein and BRD binding sites (Kundu et al., 2015; Doukas et al., 2007).

In conclusion, our findings establish a causal link between null mutations in *taf1* and *taf5*, phenotypes present in TAFopathy patients, and perturbations in metabolism and cell cycle-related pathways. These findings provide exciting and novel insights into how components of general transcription machinery selectively regulate specific transcriptional programs and contribute to tissue and organ maturation during embryonic development.

MATERIALS AND METHODS

Establishment and maintenance of zebrafish lines

cora^{stl325} was generated through an ENU mutagenesis screen (de Bruijn et al., 2009). Transgenic reporter lines such as *Tg(cmlc2:GFP)* were obtained from other labs (Huang et al., 2003). *taf5^{stl852/stl852}*, *taf5^{stl851/stl851}* *taf1^{stl456/stl456}* lines were generated using CRISPR/Cas9-mediated mutagenesis. Using a guide RNA targeting exon 1 of TAF5 (gRNA sequence: GGCTGCGGTGAGTGCGCATGAGG), we deleted a ~2.5 kb region spanning exons 1 and 2. *taf5^{stl851}* was generated using CRISPR/Cas9 (gRNA sequence: GGTGTCCGCGCCCCGTGTCAGG) to create a 17 bp deletion that resulted in a nonsense mutation. Lastly, *taf1^{stl456}* was generated by using a gRNA targeting exon 7 that created a 19 bp insertion resulting in a nonsense mutation (gRNA sequence: GGTGTCCGCGCCCCGTGTCAGG). These larvae were grown and selected based on genotype, all of which was based on existing protocols (Li et al., 2016). Genotyping of *corazoncito* exon 3 was performed using the primers 5'-ATGCGTCATGACGTAATCACATCCAGC-3' and 5'-TCACTGGGAGTTGTAGAGCCTGCGGC-3', which amplified a 333-bp region including the *corazoncito* mutation, using the restriction enzyme HpyCh4III (NEB; cat. No. R0618) that bifurcates the amplicon into ~161-bp doublets. All lines used in this study were raised and maintained by Washington University's Fish Facility. A summary of their zebrafish husbandry guidelines can be found here (<https://zebrafishfacility.wustl.edu/facility-documents/>).

Microscopy experiments

Brightfield microscopy images were taken using a Leica M80 Microscope with a mounted Leica IC80 HD camera. Fish were anesthetized in 20-30 mg/L of Tricaine in E3 water and positioned for imaging. Measurements of cartilaginous structures, head and eye components, ejection fraction and pericardium were performed with ImageJ (Collins, 2007). Ejection fraction was measured by measuring the area of the ventricle at systole and diastole. We used these area measurements to find the difference in area, which was then divided by the ventricle area during diastole.

Fluorescence microscopy was performed using a Zeiss Lightsheet 7 in the Washington University Center for Cellular imaging (WUCCI). Sample preparation protocol can be found here (https://www.iob.uu.se/digitalAssets/576/c_576400-1_1-k_protocol-for-lightsheet-z.1-using-zebrafish.pdf). For Zeiss lightsheet microscopy, larvae were anesthetized in 20-30 mg/L of Tricaine in E3 water, and then placed in a 1% low-melting agarose solution. This larvae/agarose combination was then inserted into a black glass capillary, after which larvae hearts were imaged.

X-ray microscopy was performed using a Zeiss Xradia Versa 520 XRM microscope at WUCCI (Bayguinov et al., 2020). Zebrafish larvae were fixed in 4% paraformaldehyde, then transferred to Lugol's Iodine for 3 weeks, after which samples were imaged. All imaging analysis was performed using Imaris.

Whole-mount staining

Zebrafish larvae were fixed overnight at 4°C using 4% paraformaldehyde, then washed in PBS+0.1% Tween. These embryos were then placed in 100% methanol and stored at -20°C. Alcian Blue staining was performed as previously described (Walker and Kimmel, 2007). Zebrafish larvae were imaged and staged in 100% glycerol+KOH using a Zeiss Discovery V.12 stereomicroscope.

Whole-mount *in situ* hybridization was performed according to established protocols (Cunningham and Monk, 2018). Briefly, probes were generated through PCR amplification of the coding sequences of the genes of interest using AB* cDNA libraries, followed by standard TOPO cloning (Invitrogen; cat. No. K4500) (Table S1). Transformation was performed using TOP10 chemocompetent cells (Thermo Fisher Scientific; cat. No. C505003), with confirmation of probe generation and correct orientation performed through Sanger sequencing. Once probes were validated, fixed embryos were rehydrated in a methanol/PBS gradient, permeabilized at room temperature (RT) with 10 µg/ml proteinase K, and left to fix in 4% paraformaldehyde, after which they were transferred to hybridization buffer (65% formamide, 5× SSC, 0.1% Tween, 50 µg ml⁻¹ of heparin, 500 µg ml⁻¹ of RNase-free tRNA adjusted to pH 6.0 by adding citric acid) containing 3 ng/µl probe overnight at 70°C. These embryos were then washed with hybridization buffer/PBS, followed by PBS washes, then incubated at 4°C overnight with 1:5000 anti-digoxigenin antibody (Roche, Catalog # 11093274910). Embryos were then washed with PBS and stained using BM Purple until expression could be clearly observed (Roche, Catalog # 11442074001).

Next generation sequencing and RNA sequencing

Genomic DNA and cDNA obtained from *Corazoncito* and their unaffected clutchmates was submitted to the Genome Technology Access Center for whole genome sequencing and RNA sequencing. For whole genome sequencing and mutation mapping, we used an existing pipeline as described here (Sanchez et al., 2017). Briefly, 1 µg larvae gDNA was extracted and submitted to the Genome Technology Access Center (GTAC) at Washington University for whole genome sequencing where they were bar-coded and pooled, and paired-end sequencing was performed in a single lane of a HiSeq2500 or 3000 (Illumina). Reads were aligned using NovoAlign (Novocraft), and variants were called using SAMtools. Our pipeline involved using three scripts 'ChromSplit', 'Allele Ratio Calculator' (ARC), and 'SNPFilter' to split variants into chromosome-specific data files, calculate mutant allele frequency at each point of variation between groups, and omit SNPs that have been previously annotated. Manhattan plots were generated using GraphPad Prism. Chromosomal fine mapping was performed using established markers for chromosome 1 (Table S2).

RNA sequencing pathway analysis was performed using the Shiny Transcriptome Analysis Resource Tool (Nelson et al., 2017). Pathway analysis was performed using Gene Ontology Resource (<http://geneontology.org/>). Heat maps were generated using Phantasus (<https://artyomovlab.wustl.edu/phantasus/>). FASTQ files are available (GEO GSE230183).

RT-PCR

Primers were generated through Integrated DNA Technologies' PrimerQuest tool (<https://www.idtdna.com/pages/tools/primerquest>) (Table S3). RT-PCR was performed with standard conditions. RNA was extracted from zebrafish larval tissue using the RNeasy RNA mini kit and Tissue Lyser II (Qiagen). RNA concentration was measured using a nanodrop spectrophotometer (Thermo Fisher Scientific). cDNA synthesis was performed using the High Capacity RNA to cDNA synthesis kit (Applied Biosystems). cDNA was synthesized using the iScript™ Reverse Transcription Supermix (Bio-Rad) and pre-amplified using the Sso Advanced PreAmp Supermix kit (Bio-Rad). Quantitative real time PCR reactions were prepared with sequence-specific primers (IDT) with PowerUP™ Syber Green Master mix (Thermo Fisher Scientific) in a 20 µl volume. Real time PCR was performed using QuantStudio 3 (Thermo Fisher Scientific). mRNA expression was normalized to HPRT. All RT-PCR assays were performed with appropriate quality controls including melt curves and negative controls.

Metabolism assays

Zebrafish larvae basal metabolic rate was measured in a Seahorse XF24e extracellular flux analyzer through modification of previously established protocols (Stackley et al., 2011). One 96 hpf embryo per well was used to measure the oxygen consumption rate at physiologically relevant temperature (28.5°C), with all other conditions held constant.

Targeted metabolite assays for NAD/NADH (Biovision; cat. No. K337) and ADP/ATP (Millipore-Sigma; cat. No. MAK081-1KT) were used. ATP extraction from tissues using PCA was performed according to the protocol supplied by the manufacturer. Larval tissue pools of 20 mg were flash frozen and homogenized with 200 µl of ice-cold homogenization buffer (0.25 mol L⁻¹ sucrose and 10 mmol L⁻¹ HEPES–NaOH, pH 7.4) by Tissue Lyser II (Qiagen) using one cycle of 30-s homogenization and 30-s cooling. After homogenization, the homogenate was centrifuged at 1000×g for 10 min at 4°C. One hundred microliters of the supernatant was quickly added to an equal volume of ice-cold 10% PCA and shaken for 20-s. The supernatant was then transferred into a 2.0-mL microtube for centrifugation (10,000×g for 10 min at 4°C), and 50 µl of supernatant was collected and added to 50 µl of 1 mol L⁻¹ Tris–acetate buffer (pH 7.75) for neutralization. Ten microliters of aliquot from the supernatant was used in 96-well plates for luciferin–luciferase assay, which was performed using a TECAN m200 Infinite Pro plate reader.

NAD/NADH assay samples were prepared according to the manufacturer's protocol. Twenty milligram samples of larval tissue were washed with ice cold PBS, after which 400 µl of NAD/NADH Extraction Buffer were added to the samples that were homogenized by Tissue Lyser II (Qiagen) using one cycle of 30-s homogenization and 30-s cooling. After homogenization, the homogenate was centrifuged at 24,000×g for 10 min at 4°C. Supernatant was transferred to a new tube, with 200 µl of this extract placed into a separate tube that was heated to 60°C for 30 minutes in a water bath. Both the non-decomposed and decomposed samples were added to a 96-well plate to be processed with kit reagents and OD₄₅₀ read by a TECAN m200 Infinite Pro plate reader.

Isolation of mitochondria from zebrafish embryos

For mitochondrial isolation, anesthetized pools of 100 96 hpf embryos were collected and washed in mitochondrial isolation buffer (MIB 0.21 M mannitol, 70 mM sucrose, 0.1 mM potassium-EDTA, 1 mM EGTA, 10 mM Tris-HCL, pH 7.4) for each genotype and were homogenized at 70 rpm for 20 strokes on ice in a 4 ml glass homogenizer at a ratio of 10 mg tissue per mL of MIB. The homogenate was transferred to 1.7 ml microcentrifuge tubes and centrifuged for 10 min at 600×g. Subsequently, the supernatant was centrifuged for 10 min at 7200×g to pellet mitochondria. The pellet was

then resuspended and washed twice in MIB, with the final pellet reconstituted in 500 µl of MIB.

Mitochondrial respiration assays for assessment of metabolic function

Protein concentration was determined using the BCA method per the manufacturer's instructions (Thermo Fisher Scientific). Mitochondria (300 ng protein) were placed in 2 ml mitochondria respiration buffer (MIR05: 0.5 mmol/L EGTA, 3 mmol/L MgCl₂, 60 mmol/L K-lactobionate, 20 mmol/L taurine, 10 mmol/L KH₂PO₄, 20 mmol/L HEPES, 110 mmol/L sucrose, and 1 g/L BSA [pH 7.1]) and loaded into an Oxygraph-2k respirometer (Oxygraph-2k with O2k-Fluorescence module; Oroboros Instruments, Innsbruck, Austria) at 28.5°C with continuous stirring for the measurement of O₂ flux. First, malate (1 mM) was added for depletion of endogenous substrates. Octanoylcarnitine (30 µM) was then added as a fatty acid substrate. Adenosine diphosphate (ADP; 5 mM) was added to induce state 3 respiration, with glutamate (10 mM) and succinate (10 mM) subsequently added for electron input in complex I and complex II, respectively. Cytochrome C (10 µM) was added to assess outer mitochondrial membrane integrity, and maximal oxygen flux rates were measured using chemical uncoupler carbonylcyanide-4-(trifluoromethoxy)-phenylhydrazone (FCCP), which was titrated (0.25 µM per addition) until no further stimulation of respiration could be detected.

Statistics

One-way ANOVA tests were used for ejection fraction, edema, qPCR, and metabolic experiments. Log-rank test was used for survival curves. RNA-Seq data was analyzed through START (<https://nasqar.abudhabi.nyu.edu/STARTapp/>) and Gene Ontology (<http://geneontology.org/>).

Acknowledgements

The authors are grateful to the Diabetes Research Center for providing access to their Seahorse XF24 Bioanalyzer (Supported by DRC, Grant No. P30 DK020579), Drs. Margot Williams and Diane Sepich for their kind provision of reagents, Drs. Gabe Haller and Martha Bagnell for their insights on brain anatomy, and Drs. Jun Zou and Rahul Deo for providing us with their *titin* mutant line. We thank the Genome Technology Access Center in the Department of Genetics at Washington University School of Medicine for help with genomic analysis. The Center is partially supported by NCI Cancer Center Support Grant #P30 CA91842 to the Siteman Cancer Center and by ICTS/CTSA Grant# UL1TR000448 from the National Center for Research Resources (NCRR), a component of the National Institutes of Health (NIH), and NIH Roadmap for Medical Research. This publication is solely the responsibility of the authors and does not necessarily represent the official view of NCRR or NIH. Experiments, data, and analysis generated from electron microscopy, Lightsheet fluorescence microscopy, and X-Ray microscopy were performed in part through the use of Washington University Center for Cellular Imaging (WUCCI) supported by Washington University School of Medicine, The Children's Discovery Institute of Washington University and St. Louis Children's Hospital (CDI-CORE-2015-505 and CDI-CORE-2019-813) and the Foundation for Barnes-Jewish Hospital (3770 and 4642).

Competing interests

The authors declare no competing or financial interests.

Author Contributions

Conceptualization: K.J.L.; Methodology: J.L., R.G., P.R., A.L.K., R.T., J.A.J.F., L.S.-K.; Formal analysis: J.L., R.G., P.R., A.L.K., R.T.; Investigation: J.L.; Resources: R.G., J.A.J.F., C.K., L.S.-K.; Data curation: J.L.; Writing - original draft: J.L., K.J.L.; Writing - review & editing: J.L., R.G., C.K., L.S.-K., K.J.L.; Visualization: J.L., J.A.J.F.; Supervision: L.S.-K., K.J.L.; Project administration: L.S.-K., K.J.L.; Funding acquisition: K.J.L.

Funding

K.J.L. is supported by funding provided from the Children's Discovery Institute of Washington University and St. Louis Children's Hospital, Foundation for Barnes-Jewish Hospital, Burroughs Foundation Welcome Fund, Leducq Foundation, National Institutes of Health (NIH) (HL138466, HL139714, HL151078, AI148877), and sponsored research agreements from Amgen and Novartis. J.L. is supported by an NIH F31 award (F31 HD106710-02). Open Access funding provided by Washington University School of Medicine in Saint Louis: Washington University in St Louis School of Medicine. Deposited in PMC for immediate release.

Data availability

All relevant data can be found within the article and its supplementary information.

References

- Al Ali, J., Vaine, C. A., Shah, S., Campion, L., Hakoum, A., Supnet, M. L., Acuña, P., Aldykiewicz, G., Multhaupt-Buell, T., Ganza, N. G. M. et al. (2021). TAF1 transcripts and neurofilament light chain as biomarkers for X-linked dystonia-parkinsonism. *Mov. Disord.* **36**, 206–215. doi:10.1002/mds.28305
- Alazami, A. M., Patel, N., Shamseldin, H. E., Anazi, S., Al-Dosari, M. S., Alzahrani, F., Hijazi, H., Alshammari, M., Aldahmesh, M. A., Salih, M. A. et al. (2015). Accelerating novel candidate gene discovery in neurogenetic disorders via whole-exome sequencing of prescreened multiplex consanguineous families. *Cell Rep.* **10**, 148–161. doi:10.1016/j.celrep.2014.12.015
- Aneichyk, T., Hendriks, W. T., Yadav, R., Shin, D., Gao, D., Vaine, C. A., Collins, R. L., Domingo, A., Currall, B., Stortchevoi, A. et al. (2018). Dissecting the causal mechanism of X-linked dystonia-parkinsonism by integrating genome and transcriptome assembly. *Cell* **172**, 897–909.e21. doi:10.1016/j.cell.2018.02.011
- Ashrafian, H., Frenneaux, M. P. and Opie, L. H. (2007). Metabolic mechanisms in heart failure. *Circulation* **116**, 434–448. doi:10.1161/CIRCULATIONAHA.107.702795
- Asturias, F. J. (2009). TFIIID: a closer look highlights its complexity. *Structure* **17**, 1423–1424. doi:10.1016/j.str.2009.10.004
- Bayguinov, P. O., Fisher, M. R. and Fitzpatrick, J. A. J. (2020). Assaying three-dimensional cellular architecture using X-ray tomographic and correlated imaging approaches. *J. Biol. Chem.* **295**, 15782–15793. doi:10.1074/jbc.REV120.009633
- Bhattacharya, S., Takada, S. and Jacobson, R. H. (2007). Structural analysis and dimerization potential of the human TAF5 subunit of TFIIID. *Proc. Natl. Acad. Sci. USA* **104**, 1189–1194. doi:10.1073/pnas.0610297104
- Bieniossek, C., Papai, G., Schaffitzel, C., Garzoni, F., Chaillet, M., Scheer, E., Papadopoulos, P., Tora, L., Schultz, P. and Berger, I. (2013). The architecture of human general transcription factor TFIIID core complex. *Nature* **493**, 699–702. doi:10.1038/nature11791
- Brou, C., Kuhn, A., Staub, A., Chaudhary, S., Grummt, I., Davidson, I. and Tora, L. (1993). Sequence-specific transactivators counteract topoisomerase II-mediated inhibition of in vitro transcription by RNA polymerases I and II. *Nucleic Acids Res.* **21**, 4011–4018. doi:10.1093/nar/21.17.4011
- Capponi, S., Stöffler, N., Penney, E. B., Grütz, K., Nizamuddin, S., Vermunt, M. W., Castelijn, B., Fernandez-Cerado, C., Legarda, G. P., Velasco-Andrada, M. S. et al. (2021). Dissection of TAF1 neuronal splicing and implications for neurodegeneration in X-linked dystonia-parkinsonism. *Brain Commun.* **3**, fcab253. doi:10.1093/braincomms/fcab253
- Chen, Z.-Z., Gao, Y.-Q., Xie, H., Huang, Y.-C., Chen, F. and Lei, Y.-P. (2022). Transcription factors dysregulated in three complex birth defects datasets. *Reprod. Dev. Med.* **6**, 79–85. doi:10.1097/RD9.0000000000000018
- Clark, K. L., Yutzey, K. E. and Benson, D. W. (2006). Transcription factors and congenital heart defects. *Annu. Rev. Physiol.* **68**, 97–121. doi:10.1146/annurev.physiol.68.040104.113828
- Collins, T. J. (2007). ImageJ for microscopy. *BioTechniques* **43**, S25–S30. doi:10.2144/000112517
- Cunningham, R. L. and Monk, K. R. (2018). Whole mount in situ hybridization and immunohistochemistry for zebrafish larvae. *Methods Mol. Biol.* **1739**, 371–384. doi:10.1007/978-1-4939-7649-2_25
- De Bruijn, E., Cuppen, E. and Feitsma, H. (2009). Highly efficient ENU mutagenesis in zebrafish. *Methods Mol. Biol.* **546**, 3–12. doi:10.1007/978-1-60327-977-2_1
- De Soysa, T. Y., Ranade, S. S., Okawa, S., Ravichandran, S., Huang, Y., Salunga, H. T., Schrick, A., Del Sol, A., Gifford, C. A. and Srivastava, D. (2019). Single-cell analysis of cardiogenesis reveals basis for organ-level developmental defects. *Nature* **572**, 120–124. doi:10.1038/s41586-019-1414-x
- Doukas, J., Wrasidlo, W., Noronha, G., Dneprovskaia, E., Hood, J. and Soll, R. (2007). Isoform-selective PI3K inhibitors as novel therapeutics for the treatment of acute myocardial infarction. *Biochem. Soc. Trans.* **35**, 204–206. doi:10.1042/BST0350204
- Gangloff, Y.-G., Werten, S., Romier, C., Carré, L., Poch, O., Moras, D. and Davidson, I. (2000). The human TFIIID components TAF(II)135 and TAF(II)20 and the yeast SAGA components ADA1 and TAF(II)68 heterodimerize to form histone-like pairs. *Mol. Cell. Biol.* **20**, 340–351. doi:10.1128/MCB.20.1.340-351.2000
- Gray, R. S., Gonzalez, R., Ackerman, S. D., Minora, R., Grist, J. F., Bayrak, M. N., Troutwine, B., Canter, S., Monk, K. R., Sepich, D. S. et al. (2021). Postembryonic screen for mutations affecting spine development in zebrafish. *Dev. Biol.* **471**, 18–33. doi:10.1016/j.ydbio.2020.11.009
- Grune, J., Lewis, A. J., Yamazoe, M., Hulsmans, M., Rohde, D., Xiao, L., Zhang, S., Ott, C., Calcagno, D. M., Zhou, Y. et al. (2022). Neutrophils incite and macrophages avert electrical storm after myocardial infarction. *Nat. Cardiovasc. Res.* **1**, 649–664. doi:10.1038/s44161-022-00094-w
- Gudmundsson, S., Wilbe, M., Filipek-Górniok, B., Molin, A.-M., Ekvall, S., Johansson, J., Allalou, A., Gylje, H., Kalscheuer, V. M., Ledin, J. et al. (2019). TAF1, associated with intellectual disability in humans, is essential for embryogenesis and regulates neurodevelopmental processes in zebrafish. *Sci. Rep.* **9**, 10730. doi:10.1038/s41598-019-46632-8
- Hellman-Aharony, S., Smirin-Yosef, P., Halevy, A., Pasmanik-Chor, M., Yeheskel, A., Har-Zahav, A., Maya, I., Straussberg, R., Dahary, D., Haviv, A. et al. (2013). Microcephaly thin corpus callosum intellectual disability syndrome caused by mutated TAF2. *Pediatr. Neurol.* **49**, 411–416.e1. doi:10.1016/j.pediatrneurol.2013.07.017
- Huang, C.-J., Tu, C.-T., Hsiao, C.-D., Hsieh, F.-J. and Tsai, H.-J. (2003). Germ-line transmission of a myocardium-specific GFP transgene reveals critical regulatory elements in the cardiac myosin light chain 2 promoter of zebrafish. *Dev. Dyn.* **228**, 34–40. doi:10.1002/dvdy.10356
- Jacobson, R. H., Ladurner, A. G., King, D. S. and Tjian, R. (2000). Structure and function of a human TAFII250 double bromodomain module. *Science* **288**, 1422–1425. doi:10.1126/science.288.5470.1422
- Jenkins, K. J., Correa, A., Feinstein, J. A., Botto, L., Britt, A. E., Daniels, S. R., Elixson, M., Warnes, C. A. and Webb, C. L. (2007). Noninherited risk factors and congenital cardiovascular defects: current knowledge: a scientific statement from the American Heart Association Council on Cardiovascular Disease in the Young: endorsed by the American Academy of Pediatrics. *Circulation* **115**, 2995–3014. doi:10.1161/CIRCULATIONAHA.106.183216
- Juven-Gershon, T. and Kadonaga, J. T. (2010). Regulation of gene expression via the core promoter and the basal transcriptional machinery. *Dev. Biol.* **339**, 225–229. doi:10.1016/j.ydbio.2009.08.009
- Juven-Gershon, T., Cheng, S. and Kadonaga, J. T. (2006). Rational design of a super core promoter that enhances gene expression. *Nat. Methods* **3**, 917–922. doi:10.1038/nmeth937
- Kaufman, C. K., Mosimann, C., Fan, Z. P., Yang, S., Thomas, A. J., Ablain, J., Tan, J. L., Fogley, R. D., Van Rooijen, E., Hagedorn, E. J. et al. (2016). A zebrafish melanoma model reveals emergence of neural crest identity during melanoma initiation. *Science* **351**, aad2197. doi:10.1126/science.aad2197
- Kirby, R. S. (2017). The prevalence of selected major birth defects in the United States. *Semin. Perinatol.* **41**, 338–344. doi:10.1053/j.semper.2017.07.004
- Kloet, S. L., Whiting, J. L., Gafken, P., Ranish, J. and Wang, E. H. (2012). Phosphorylation-dependent regulation of cyclin D1 and cyclin A gene transcription by TFIIID subunits TAF1 and TAF7. *Mol. Cell. Biol.* **32**, 3358–3369. doi:10.1128/MCB.00416-12
- Kundu, B. K., Zhong, M., Sen, S., Davogustto, G., Keller, S. R. and Taegtmeier, H. (2015). Remodeling of glucose metabolism precedes pressure overload-induced left ventricular hypertrophy: review of a hypothesis. *Cardiology* **130**, 211–220. doi:10.1159/000369782
- Lehmann, L., Ferrari, R., Vashisht, A. A., Wohlschlegel, J. A., Kurdistani, S. K. and Carey, M. (2012). Polycomb repressive complex 1 (PRC1) disassembles RNA polymerase II preinitiation complexes. *J. Biol. Chem.* **287**, 35784–35794. doi:10.1074/jbc.M112.397430
- Li, M., Zhao, L., Page-McCaw, P. S. and Chen, W. (2016). Zebrafish genome engineering using the CRISPR-Cas9 system. *Trends Genet.* **32**, 815–827. doi:10.1016/j.tig.2016.10.005
- Louder, R. K., He, Y., López-Blanco, J. R., Fang, J., Chacón, P. and Nogales, E. (2016). Structure of promoter-bound TFIIID and model of human pre-initiation complex assembly. *Nature* **531**, 604–609. doi:10.1038/nature17394
- Nechiporuk, A., Finney, J. E., Keating, M. T. and Johnson, S. L. (1999). Assessment of polymorphism in zebrafish mapping strains. *Genome Res.* **9**, 1231–1238. doi:10.1101/gr.9.12.1231
- Nelson, J. W., Sklenar, J., Barnes, A. P. and Minnier, J. (2017). The START App: a web-based RNAseq analysis and visualization resource. *Bioinformatics* **33**, 447–449. doi:10.1093/bioinformatics/btw624
- O'Rawe, J. A., Wu, Y., Dörfel, M. J., Rope, A. F., Au, P. Y. B., Parboosingh, J. S., Moon, S., Kousi, M., Kosma, K., Smith, C. S. et al. (2015). TAF1 Variants Are Associated with Dysmorphic Features, Intellectual Disability, and Neurological Manifestations. *Am. J. Hum. Genet.* **97**, 922–932. doi:10.1016/j.ajhg.2015.11.005
- Oelgeschläger, T., Tao, Y., Kang, Y. K. and Roeder, R. G. (1998). Transcription activation via enhanced preinitiation complex assembly in a human cell-free system lacking TAFII. *Mol. Cell* **1**, 925–931. doi:10.1016/S1097-2765(00)80092-1
- Patel, A. B., Louder, R. K., Greber, B. J., Grünberg, S., Luo, J., Fang, J., Liu, Y., Ranish, J., Hahn, S. and Nogales, E. (2018). Structure of human TFIIID and mechanism of TBP loading onto promoter DNA. *Science* **362**, eaau8872. doi:10.1126/science.aau8872
- Prescott, K. R. and Wilkie, A. O. M. (2007). Genetic aspects of birth defects: new understandings of old problems. *Arch. Dis. Child. Fetal Neonatal Ed.* **92**, F308–F314. doi:10.1136/adc.2004.062968
- Rhee, H. S. and Pugh, B. F. (2012). Genome-wide structure and organization of eukaryotic pre-initiation complexes. *Nature* **483**, 295–301. doi:10.1038/nature10799
- Roeder, R. G. (1996). The role of general initiation factors in transcription by RNA polymerase II. *Trends Biochem. Sci.* **21**, 327–335. doi:10.1016/0968-0004(96)10050-5
- Rooms, L., Reyniers, E., Scheers, S., Van Lwijk, R., Wauters, J., Van Aerscht, L., Callaerts-Vegh, Z., D'hooge, R., Mengus, G., Davidson, I. et al. (2006). TBP

- as a candidate gene for mental retardation in patients with subtelomeric 6q deletions. *Eur. J. Hum. Genet.* **14**, 1090-1096. doi:10.1038/sj.ejhg.5201674
- Sanchez, N. E., Harty, B. L., O'Reilly-Pol, T., Ackerman, S. D., Herbert, A. L., Holmgren, M., Johnson, S. L., Gray, R. S. and Monk, K. R.** (2017). Whole genome sequencing-based mapping and candidate identification of mutations from fixed zebrafish tissue. *G3* **7**, 3415-3425. doi:10.1534/g3.117.300212
- Stackley, K. D., Beeson, C. C., Rahn, J. J. and Chan, S. S. L.** (2011). Bioenergetic profiling of zebrafish embryonic development. *PLoS One* **6**, e25652. doi:10.1371/journal.pone.0025652
- Tawamie, H., Martianov, I., Wohlfahrt, N., Buchert, R., Mengus, G., Uebe, S., Janiri, L., Hirsch, F. W., Schumacher, J., Ferrazzi, F. et al.** (2017). Hypomorphic pathogenic variants in TAF13 are associated with autosomal-recessive intellectual disability and microcephaly. *Am. J. Hum. Genet.* **100**, 555-561. doi:10.1016/j.ajhg.2017.01.032
- Walker, M. B. and Kimmel, C. B.** (2007). A two-color acid-free cartilage and bone stain for zebrafish larvae. *Biotech. Histochem.* **82**, 23-28. doi:10.1080/10520290701333558
- Wang, H., Curran, E. C., Hinds, T. R., Wang, E. H. and Zheng, N.** (2014). Crystal structure of a TAF1-TAF7 complex in human transcription factor IID reveals a promoter binding module. *Cell Res.* **24**, 1433-1444. doi:10.1038/cr.2014.148
- Webber, D. M., Macleod, S. L., Bamshad, M. J., Shaw, G. M., Finnell, R. H., Shete, S. S., Witte, J. S., Erickson, S. W., Murphy, L. D. and Hobbs, C.** (2015). Developments in our understanding of the genetic basis of birth defects. *Birth Defects Res. A Clin. Mol. Teratol.* **103**, 680-691. doi:10.1002/bdra.23385
- Wu, S. Y. and Chiang, C. M.** (2001). TATA-binding protein-associated factors enhance the recruitment of RNA polymerase II by transcriptional activators. *J. Biol. Chem.* **276**, 34235-34243. doi:10.1074/jbc.M102463200
- Xu, Y., Man, N., Karl, D., Martinez, C., Liu, F., Sun, J., Martinez, C. J., Martin, G. M., Beckedorff, F., Lai, F. et al.** (2019). TAF1 plays a critical role in AML1-ETO driven leukemogenesis. *Nat. Commun.* **10**, 4925. doi:10.1038/s41467-019-12735-z
- Zou, J., Tran, D., Baalbaki, M., Tang, L. F., Poon, A., Pelonero, A., Titus, E. W., Yuan, C., Shi, C., Patchava, S. et al.** (2015). An internal promoter underlies the difference in disease severity between N- and C-terminal truncation mutations of Titin in zebrafish. *Elife* **4**, e09406. doi:10.7554/eLife.09406